

**P3HT:PCBM-BASED ORGANIC SOLAR CELLS
INCORPORATED WITH SOLID ADDITIVES FOR
INDOOR PHOTOVOLTAIC APPLICATIONS**

**SHAWBO ABDULSAMAD ABUBAKER
ABUBAKER**

UNIVERSITI SAINS MALAYSIA

2025

**P3HT:PCBM-BASED ORGANIC SOLAR CELLS
INCORPORATED WITH SOLID ADDITIVES FOR
INDOOR PHOTOVOLTAIC APPLICATIONS**

by

**SHAWBO ABDULSAMAD ABUBAKER
ABUBAKER**

**Thesis submitted in fulfilment of the requirements
for the degree of
Doctor of Philosophy**

May 2025

ACKNOWLEDGEMENT

In the Name of Allah, Most Gracious, Most Merciful. First and foremost, I am deeply grateful to Allah Almighty for granting me the strength, knowledge, and perseverance to complete this research. Without His guidance and blessings, this work would not have been possible.

I dedicate this thesis to the cherished memory of my beloved father, who passed away this year, just as I neared the completion of this journey. His endless love, patience, and prayers have been my constant guiding light, offering me strength and comfort through every challenge. My father's unwavering belief in my potential and his deepest wish for me to achieve this PhD have motivated me every step of the way. I hope this accomplishment not only honours his memory but also fulfils the dream he so dearly held in his heart. I am thankful to my dear mother, brothers, and sisters for their endless love and prayers.

My heartfelt appreciation goes to my supervisor, **Associate Professor Ts. Dr. Mohd Zamir bin Pakhuruddin**, for his invaluable guidance, continuous support, and encouragement throughout this project. Their profound knowledge and insightful feedback have greatly contributed to the quality and completion of this thesis. I also extend my sincere gratitude to my co-supervisor, **Dr. Marzaini Rashid**, for his valuable assistance and support.

Lastly, I extend my gratitude to my colleagues and friends, who offered their support, and everyone who has contributed to this work, directly or indirectly. May Allah reward you all for your kindness and support.

Shawbo Abdulsamad

TABLE OF CONTENTS

ACKNOWLEDGEMENT	ii
TABLE OF CONTENTS	iii
LIST OF TABLES	ix
LIST OF FIGURES	x
LIST OF SYMBOLS	xix
LIST OF ABBREVIATIONS	xx
ABSTRAK	xxi
ABSTRACT	xxiii
CHAPTER 1 INTRODUCTION	1
1.1 Introduction	1
1.2 Problem statement	6
1.3 Research focus.....	8
1.4 Research objectives	9
1.5 Thesis outline	9
CHAPTER 2 THEORETICAL BACKGROUND AND LITERATURE REVIEW	11
2.1 Introduction	11
2.2 Generations of solar cell.....	11
2.3 Organic solar cells (OSCs).....	13
2.4 OSC device architecture	16
2.4.1 Bulk heterojunction OSCs.....	18
2.4.2 Buffer layers in OSCs	19
2.4.3 Electrodes in OSCs.....	22
2.5 Operation of OSCs	24
2.5.1 Short circuit current density (J_{sc}).....	29

2.5.2	Open circuit voltage (V_{OC}).....	29
2.5.3	Series (R_S) and shunt resistance (R_{Sh}).....	30
2.5.4	Fill Factor (FF).....	31
2.5.5	Power conversion efficiency (PCE).....	31
2.6	Indoor photovoltaics (IPV).....	32
2.7	IPV based on organic materials.....	36
2.8	Challenges of OSCs	45
2.8.1	Power conversion efficiencies.....	45
2.8.1(a)	Photon absorption and photoactive layer thickness.....	46
2.8.1(b)	Charge carrier imbalance	48
2.8.2	Stability	48
2.8.2(a)	Morphology	51
2.8.2(b)	Buffer layers	55
2.8.2(c)	The diffusion of metal electrodes	56
2.8.2(d)	Moisture-induced degradation.....	57
2.8.2(e)	Heating effects	58
2.8.2(f)	Mechanical stress.....	59
2.9	Role of additives.....	60
2.9.1	Solvent additives	61
2.9.2	Solid additives	63
2.9.3	Classification of solid additives	66
2.9.4	Device design with solid additives.....	72
CHAPTER 3 MATERIALS AND METHODOLOGY		76
3.1	Introduction	76
3.2	Materials.....	77
3.3	Thin film deposition and OSCs fabrication.....	79
3.3.1	Substrates etching and cleaning	79

3.3.2	Preparation of P3HT:PCBM based OSCs	80
3.3.2(a)	Effect of different volume ratios of P3HT polymer and acceptor PCBM	80
3.3.2(b)	Effect of spin coating speed.....	81
3.3.2(c)	Effect of annealing temperature.....	81
3.3.2(d)	Effect of annealing time.....	81
3.4	Preparation of PEDOT:PSS with different volume ratios of 2,3-DHP	82
3.5	Preparation of P3HT:PCBM with different volume ratios of 2,3-DHP	84
3.6	Preparation of modified HTLs and active layers with 2,3-DHP	86
3.7	Preparation of modified ETLs	87
3.7.1	Synthesis of ZnO NPs	88
3.7.2	Synthesis of Alq3 Compound	88
3.7.3	Synthesis of ZnO NPs:Alq3	88
3.8	Preparation of thin film and metal contact deposition	89
3.9	Thin film processing.....	91
3.9.1	Oxygen plasma treatment.....	91
3.9.2	Thermal evaporation	92
3.9.3	Spin coating method.....	94
3.10	Characterization techniques	95
3.10.1	Ultraviolet-visible-near infrared (UV-Vis-NIR) spectrometer	95
3.10.2	X-ray diffraction (XRD).....	97
3.10.3	Fourier transform infrared spectroscopy (FTIR).....	99
3.10.4	Field emission scanning electron microscope (FESEM)	100
3.10.5	Atomic force microscopy (AFM).....	101
3.10.6	Hall effect measurement (HEM)	102
3.10.7	Four-point probe (FPP)	103
3.10.8	Solar simulator	104

CHAPTER 4	RESULTS AND DISCUSSION.....	105
4.1	Introduction	105
4.2	Optimization of P3HT:PCBM based OSCs	105
4.2.1	Optical properties	105
4.2.1(a)	UV-Vis-NIR spectroscopy.....	105
4.2.2	Surface morphological properties	110
4.2.2(a)	AFM analysis.....	110
4.2.2(b)	FESEM analysis.....	116
4.2.3	Structural properties	120
4.2.3(a)	XRD analysis	120
4.2.3(b)	FTIR analysis.....	121
4.2.4	Electrical properties.....	122
4.2.4(a)	Extraction of device electrical resistivity and conductivity	122
4.3	Optimization of PEDOT:PSS with different volume ratios of 2,3-DHP	124
4.3.1	Optical properties	124
4.3.1(a)	UV-Vis-NIR spectroscopy.....	124
4.3.2	Surface morphological properties	128
4.3.2(a)	AFM analysis.....	128
4.3.2(b)	FESEM analysis.....	130
4.3.3	Structural properties	133
4.3.3(a)	XRD analysis	133
4.3.3(b)	FTIR analysis.....	134
4.3.4	Electrical properties.....	136
4.3.4(a)	Extraction of device electrical resistivity and conductivity	136
4.4	Optimization of P3HT:PCBM with different volume ratios of 2,3-DHP	138
4.4.1	Optical properties	138

4.4.1(a)	UV-Vis-NIR spectroscopy.....	138
4.4.2	Surface morphological properties	142
4.4.2(a)	AFM analysis.....	142
4.4.2(b)	FESEM analysis.....	147
4.4.3	Structural properties	150
4.4.3(a)	XRD analysis	150
4.4.3(b)	FTIR analysis.....	151
4.4.4	Electrical properties.....	152
4.4.4(a)	Extraction of device electrical conductivity	152
4.5	Improved OSC performance with modified ETLs	153
4.5.1	Optical properties	153
4.5.1(a)	UV-Vis-NIR spectroscopy.....	153
4.5.2	Surface morphological properties	155
4.5.2(a)	AFM analysis.....	155
4.5.2(b)	FESEM analysis.....	157
4.5.3	Structural properties	159
4.5.3(a)	XRD analysis	159
4.5.3(b)	FTIR analysis.....	161
4.5.4	Electrical properties.....	162
4.5.4(a)	Extraction of device electrical conductivity	162
4.6	Optimization of OSCs performance with modified HTLs and active layer conditions	164
4.6.1	Optical properties	164
4.6.1(a)	UV-Vis-NIR spectroscopy.....	164
4.6.2	Surface morphological properties	166
4.6.2(a)	AFM analysis.....	166
4.6.2(b)	FESEM analysis.....	168
4.6.3	Electrical properties.....	170

4.6.3(a)	Extraction of device electrical conductivity	170
4.7	OSCs performance	171
4.7.1	Improved OCSs performance by enhancing P3HT:PCBM-BHJ	171
4.7.2	Enhancing HTL of OSCs with 2,3-DHP	174
4.7.3	Enhancing P3HT:PCBM BHJ with 2,3-DHP	177
4.7.4	Enhancing OSCs with various ETLs.....	179
4.7.5	Enhanced OSCs based on modified HTL and P3HT:PCBM BHJ film through solid additives	184
4.7.6	Indoor light intensity effect on OSCs.....	187
CHAPTER 5 CONCLUSIONS AND FUTURE RECOMMENDATIONS .		193
5.1	Conclusion.....	193
5.2	Contribution of the thesis	195
5.3	Recommendations for Future Research	196
REFERENCES.....		198
LIST OF PUBLICATIONS		

LIST OF TABLES

		Page
Table 2.1	A list of experiments on IOSCs that have already been reported.	44
Table 2.2	PV performance of the OSCs with solid additives.	68
Table 4.1	RMS roughness of the various volume ratios of P3HT:PCBM films.	111
Table 4.2	RMS roughness of P3HT:PCBM films under various temperatures.	114
Table 4.3	RMS roughness of of PEDOT:PSS thin film, and doped PEDOT:PSS.	129
Table 4.4	Conductivity of PEDOT:PSS films after treatment with additives..	138
Table 4.5	RMS roughness of P3HT: PCBM-films without and with 2,3-DHP	143
Table 4.6	RMS roughness of P3HT:PCBM:2,3-DHP based films under various temperatures.	144
Table 4.7	RMS roughness of ZnO NPs, Alq3, ZnO NPs:Alq3 on active layer.....	156
Table 4.8	RMS roughness of no additive and additive (2,3-DHP) in HTL and the active layer.	167
Table 4.9	PV parameters of various volume ratios of P3HT and PCBM.	172
Table 4.10	PV parameters of various HTLs with and without 2,3-DHP.	176
Table 4.11	P3HT:PCBM with and without solid additive 2,3-DHP parameters of the fabricated OSCs.	179
Table 4.12	Parameters of OSC devices without and with various ETLs.	183
Table 4.13	Parameters of fabrication OSCs with and without additives in HTL and active layer respectively.	186
Table 4.14	OSCs parameters under various light intensities.	191

LIST OF FIGURES

	Page
Figure 1.1	Various renewable energy resources and solar energy conversion into electricity by different generations of PV technologies..... 1
Figure 1.2	Absorption coefficients of utilized donor and acceptor materials [8].....2
Figure 1.3	Standard household and personal electronics and common wireless network protocols, all contribute to low power usage.3
Figure 1.4	Different light spectra: solar spectrum (AM1.5G), white LED, CFL, and Halogen sources [15].4
Figure 1.5	Market size of IOPV in billions of dollars [19].5
Figure 1.6	Schematic device illustration of the research focus of this thesis.....9
Figure 2.1	Generations of photovoltaics and their types. The maximum reported efficiency, taken from the NREL database [38]. 12
Figure 2.2	The best solar cell efficiency [59]..... 16
Figure 2.3	The OSC configurations..... 17
Figure 2.4	(a) OSC device configuration, (b) Blend of the BHJ active layer. 18
Figure 2.5	Device architecture for (a) Conventional, and (b) Inverted OSCs..... 19
Figure 2.6	Factors for enhancing buffer layers in OSCs.20
Figure 2.7	Mechanisms of using electrodes for efficient OSCs.....23
Figure 2.8	Energy band diagram for an OSC.25
Figure 2.9	Incident power density vs illuminance for various light sources [110].26
Figure 2.10	Schematic diagram of the density of states in the donor and acceptor materials under strong and low illumination intensity [112].27
Figure 2.11	Current density versus voltage characteristic of OSC.....29

Figure 2.12	The tailored bandgap of various devices, (a) J–V curves under 1 sun illumination,(b) J–V curves under 1000 lux indoor light, (c) The statistics of PCE, (d) SEM cross-sectional view [141].	35
Figure 2.13	PCE under AM1.5G and indoor illumination for different PVs [142].	36
Figure 2.14	Several chemical structures of polymers, fullerene, and non-fluorene materials are used in high-performance IPVs [148].	38
Figure 2.15	Schematic representation of energy levels in different donor-acceptor combinations [158], (b) Energy level diagram of the ternary component [159].	40
Figure 2.16	(a) Device structure, (b) J- V_{oc} of pure and doped devices under different illumination, (c) IPCE under 1-sun illumination, (d) J-V curve for pure and doped devices under white LED [160].	40
Figure 2.17	J-V curve of various BHJ devices under (a) AM 1.5G and (b) fluorescent lamp illumination [145], (c) V_{oc} under 1-Sun and 300 lux of illumination conditions [163].	42
Figure 2.18	(a) Charge transfer mechanism in quaternary OPV, (b) J-V curves, (c) V_{oc} as a function of light-intensity plot, (d) J- V_{eff} of the binary, ternary, and quaternary devices [165].	43
Figure 2.19	(a) Device structure of OSC based on P3HT:ICBA [161], (b-c) and (d) FF, V_{oc} , J_{sc} , and PCE of the cells under two lighting conditions [179].	47
Figure 2.20	Factors affecting the stability of OSC cells.....	49
Figure 2.21	(a) V_{oc} vs time under 1 sun, (b) Raman spectra of PEDOT:PSS and doped PEDOT:PSS [184].	50
Figure 2.22	(a) OSC device configuration, (b) The influence of annealing on solar cell properties, pre-annealed, and post-annealed P3HT:PCBM solar cells, and (C) EQE as a function of wavelength for P3HT-I:PCBM [199].	52

Figure 2.23	Schematic diagram of energy levels converting photons to photocurrent in OSCs.....	54
Figure 2.24	Schematic illustration of the degradation mechanism of OSCs with humidity [225].....	57
Figure 2.25	Illustration of how mechanical stress, like punctures, strains, and delamination, can cause mechanical damage [189].	59
Figure 2.26	Advantages of additives in OSCs.....	61
Figure 2.27	Solvent additives for BHJ OSCs [196].	63
Figure 2.28	The impact of SAs on blend morphology, (a) PM6, (b) Y6, and (c) PM6:Y6 films processed with varying percentages of DIB, including 0%, 100% (100wt%), 200% (200wt%), and 300% (300wt%) [263].	64
Figure 2.29	(a) Schematic of the OSC with solid additives (Star-A and Star-F) and solvent additive (1-CN), (b) Schematic of the effect of introducing solid-solvent hybrid additives in blend systems [265]. ..	65
Figure 2.30	(a) The chemical structures of non-volatile solid additives, (b) Chemical structures of volatile solid additives, (c) Schematic diagram illustrating the working mechanism of 2,3 DHP non-volatile solid additives treatment [271], (d) Schematic diagram of the working mechanism of SA-1 treatment [266].....	67
Figure 2.31	(a) Chemical structures of non-volatile solid additives, (b) J-V curves of DDO and DIO co-doped devices with different doping ratios, (c) EQE curves of OSCs with different concentrations of DIO and DDO [284].....	70
Figure 2.32	AFM images of the optimized device photoactive layers (a) without, and with (b) MONs [286].	71
Figure 2.33	AFM images of the optimized device photoactive layers (a) without, and with (b) MONs [286].	72
Figure 2.34	Different design strategies for enhancing OSCs with solid additives.	73

Figure 2.35	(a) Solid additive molecules induce a conformational transformation in the chains of PEDOT:PSS structure, (b) Conductivity of PEDOT:PSS films, and (c) The (J-V) curve with varying concentrations of DOH [292].	74
Figure 2.36	(a) A diagram illustrating the structure of the device, (b) The J-V curve, (c) The PL of P3HT:ICBA and P3HT:ICBA:DHP thin films, and (d) AFM images of P3HT:ICBA with and without DHP [273].	75
Figure 3.1	Flow chart of the experimental steps.	77
Figure 3.2	The main materials used in the current research.	78
Figure 3.3	Etching and cleaning of ITO/glass substrate.	80
Figure 3.4	Glovebox inside which active layer films were prepared.	80
Figure 3.5	Schematic illustration of the preparation and synthesis solution-based P3HT:PCBM active layer.	81
Figure 3.6	Schematic illustration of preparation, synthesis, and annealing P3HT:PCBM blend.	82
Figure 3.7	Schematic illustration of PEDOT:PSS@2,3-DHP thin films preparation.	83
Figure 3.8	The diagrams illustrate (a) the structure of PEDOT:PSS, (b) 2,3-DHP, (c) the formation of hydrogen bonds, and (d) the annealing and expansion procedures of PEDOT:PSS in the presence of 2,3-DHP.	84
Figure 3.9	Schematic illustration of preparation, synthesis P3HT:PCBM:2,3-DHP active layer.	85
Figure 3.10	The diagrams illustrate the structure of P3HT and PCBM and their bonds with 2,3-DHP.	86
Figure 3.11	A digital photograph of active layer solution and coated film.	87
Figure 3.12	The schematic diagram for preparing ZnO NPs:Alq3 nanocomposite thin films.	89
Figure 3.13	Fabrication of OSC device.	89

Figure 3.14	Image and schematic diagram of the fabricated OSC.....	91
Figure 3.15	Plasma treatment device (PLASMAPREP 100).....	91
Figure 3.16	(a) Image and (b) Schematic diagram of the thermal evaporation system.....	93
Figure 3.17	Schematic of spin-coating process.....	94
Figure 3.18	(a) A digital photograph of UV-Vis-NIR spectrophotometer, (b) Working principle illustration of the UV-Vis-NIR system [294].	96
Figure 3.19	(a) Image of XRD system (PANalytical X'pert PRO MRD PW3040/60), (b) Bragg's condition [297].	98
Figure 3.20	(a) FTIR spectrophotometer, and (b) Its working principle [298].	99
Figure 3.21	(a) FESEM system (Model: FEI Nova NanoSEM 450), (b) Schematic demonstration of the operating principle [299].	101
Figure 3.22	(a) AFM image (b) Schematic illustrating the working principle of AFM [300].	102
Figure 3.23	Hall effect measurement.....	103
Figure 3.24	Four-point probe (FPP) device.....	103
Figure 3.25	Solar simulator measurement system (Forster Transient Measurement System) for evaluating PCE of the fabricated OSCs.	104
Figure 4.1	The energy bandgap determination for the P3HT: PCBM-based films prepared by the different volume ratios of polymer and florent-based acceptors.....	106
Figure 4.2	Absorption spectra of the P3HT: PCBM-based films for (a) various volume ratios of donor P3HT and acceptor PCBM, (b) different spin coating, (c) different temperatures, and (d) different annealing times.	108
Figure 4.3	FESEM cross-sectional image of the optimized OSCs.....	109
Figure 4.4	AFM images of P3HT:PCBM films with various volume ratios: (a) 2:1, (b) 1:1, and (c) 1:2.....	112

Figure 4.5	AFM images of P3HT:PCBM films under various temperatures: (a) Ref, (b) 100 °C, (c) 120 °C, (d) 140 °C, and (d) 160 °C.	116
Figure 4.6	FESEM images of P3HT: PCBM films with various volume ratios: (a) 2:1, (b) 1:1, (c) 1:2.	117
Figure 4.7	FESEM images of P3HT:PCBM films under various temperatures: (a) Ref, (b) 100 °C, (c) 120 °C, (d) 140 °C, and (d) 160 °C.	119
Figure 4.8	XRD pattern of the P3HT:PCBM with various weight ratios.	121
Figure 4.9	FTIR spectra of the P3HT:PCBM with various weight ratios.	122
Figure 4.10	Resistivity as a function of various volume ratios of P3HT:PCBM film (b) Conductivity variation with various volume ratios of P3HT:PCBM, (c) Resistivity as a function of temperature, and (d) Conductivity variation with temperature.	123
Figure 4.11	(a) Transmission spectra of PEDOT:PSS with varying amounts of 2,3-DHP, (b) Absorption spectra of pristine PEDOT:PSS with various weights 2,3-DHP, (c) Refractive index, (d) Extinction coefficient and (e) Calculated energy bandgap vs energy for pure PEDOT:PSS and PEDOT:PSS@2,3DHP (1 wt%).	125
Figure 4.12	A schematic illustration of the scattered light from the HTL rough surface into the active layer to the ETL within the PV device.	128
Figure 4.13	(a) Surface topography of PEDOT:PSS thin film, (b) Surface topography of doped PEDOT:PSS treated with 1 wt% 2,3DHP, 3D-AFM images of (c) PEDOT:PSS, and (d) PEDOT:PSS@2,3- DHP.	129
Figure 4.14	(a) Surface morphological of the PEDOT:PSS thin film, (b) EDX analysis of the PEDOT:PSS thin film, (c) Surface morphological of the PEDOT:PSS@2,3-DHP (1 wt%) thin film, and (d) EDX analysis of the PEDOT:PSS@2,3-DHP (1 wt%) thin film.	132
Figure 4.15	Cross-sectional FESEM image showing the (a) glass/ITO/PEDOT:PSS thin film and (b) glass/ITO/PEDOT:PSS@2,3-DHP thin film.	133

Figure 4.16	XRD patterns of PEDOT:PSS and PEDOT:PSS with 2,3-DHP.....	134
Figure 4.17	FTIR spectra of PEDOT:PSS and PEDOT:PSS with 2,3-DHP.....	135
Figure 4.18	Average conductivity of the PEDOT:PSS films modified by 2,3-DHP pyridine-based solid additives.....	137
Figure 4.19	Absorption spectra of the active layer with a different volume ratio of 2,3-DHP.....	139
Figure 4.20	The energy bandgap determination for the P3HT:PCBM-based films prepared by 0.8 wt% volume ratio of 2,3-DHP.....	140
Figure 4.21	Absorption spectra of P3HT:PCBM:2,3-DHP with various temperature treatments.....	141
Figure 4.22	AFM images of P3HT:PCBM blend films (a) without and (b) with 2,3-DHP.....	143
Figure 4.23	AFM images of P3HT:PCBM:2,3-DHP films under various temperatures: (a) Ref, (b) 100 °C, (c) 120 °C, (d) 140 °C, and (d) 160 °C.....	147
Figure 4.24	FSEM images of (a) P3HT:PCBM, and (b) P3HT:PCBM@2,3-DHP (0.8 wt%).....	148
Figure 4.25	FESEM images of P3HT:PCBM:2,3-DHP films under various temperatures: (a) Ref, (b) 100 °C, (c) 120 °C, (d) 140 °C, and (d) 160 °C.....	149
Figure 4.26	XRD spectra of P3HT:PCBM and P3HT:PCBM:2,3-DHP blend film, respectively.....	150
Figure 4.27	FTIR spectra of P3HT:PCBM and P3HT:PCBM:2,3-DHP blend film, respectively.....	152
Figure 4.28	(a) Resistivity as a function of various volume ratios of 2,3-DHP incorporation P3HT:PCBM film (b) Conductivity variation with various volume ratios of 2,3-DHP incorporation P3HT:PCBM film.....	153
Figure 4.29	Absorption spectra of various ETLs on the active layer.....	154

Figure 4.30	AFM images of (a) ZnO NPs, (b) Alq3, and (c) ZnO NPs:Alq3 on the active layer.	157
Figure 4.31	FESEM images of (a) ZnO NPs, (b) Alq3, and (c) ZnO NPs:Alq3 on the active layer respectively.	158
Figure 4.32	XRD spectra of (a) ZnO NPs, (b) Alq3, and ZnO NPs:Alq3 on the active layer.	160
Figure 4.33	FTIR spectra of (a) ZnO NPs, (b) Alq3, and (c) ZnO NPs:Alq3 on the active layer.	162
Figure 4.34	(a) Resistivity as a function of various ETLs, (b) Conductivity variation with various ETLs.....	163
Figure 4.35	Absorption spectra of various ETLs on the active layer.....	164
Figure 4.36	AFM image of devices with (a) no additives, and (b) 2,3-DHP in HTL and the active layer.....	168
Figure 4.37	FESEM image of (a) glass/ITO/PEDOT:PSS/P3HT:PCBM, and (b) glass/ITO/PEDOT:PSS@2,3-DHP/P3HT:PCBM:2,3-DHP.	169
Figure 4.38	(a) Resistivity, (b) Conductivity of glass/ITO/PEDOT:PSS/P3HT:PCBM and glass/ITO/PEDOT:PSS@2,3-DHP /P3HT:PCBM:2,3-DHP respectively.	170
Figure 4.39	A comparison of (a) J-V and (b) power-V characteristics of various volume ratios P3HT and PCBM	174
Figure 4.40	A comparison of (a) J-V and (b) P-V characteristics of various HTLs with and without solid additive 2,3-DHP.	176
Figure 4.41	A comparison of (a) J-V and (b) P-V characteristics of P3HT:PCBM with and without 2,3-DHP.	178
Figure 4.42	Cross-sectional images of OSCs prepared, (a) Without, and (b) with 2,3-DHP.	179
Figure 4.43	A comparison of J-V and P-V characteristics of (A) Ref, (b) 2,3-DHP in PEDOT:PSS, (c) 2,3-DHP in P3HT:PCBM devices without and with various ETLs.....	182

Figure 4.44	Cross-sectional images of OSCs prepared (a) without ETL and (b) with ETL.	184
Figure 4.45	A comparison of (a) J-V and (b) P-V characteristics with and without additives in HTL and active layer, respectively.....	186
Figure 4.46	A cross-sectional of the complete device with and without additives.	187
Figure 4.47	J-V curve measurement with various intensities of LED light.	189
Figure 4.48	PCE is measured with various intensities of LED light.	189
Figure 4.49	Maximum power measurement with various intensities of LED light.	190
Figure 4.50	Maximum power measurement with various intensities of LED light.	190

LIST OF SYMBOLS

A	Absorbance
Å	Angstrom
°C	Celsius degree
E_g	Energy bandgap
eV	Electron volt
FF	Fill factor
I_{sc}	Short circuit current
I_{max}	Maximum current
mA	Milliampere
η	Efficiency
PCE	Power conversion efficiency
P_{in}	Input power
P_{out}	Output power
P_{max}	Maximum power point
R_s	Series resistance
R_{sh}	Shunt resistance
T%	Transmittance
V_{max}	Maximum voltage
V_{oc}	Open circuit voltage
W	Watt
θ	Diffraction angle
Ω	Ohm
λ	Wavelength

LIST OF ABBREVIATIONS

AFM	Atomic force microscopy
Alq3	Tris(8-hydroxyquinoline) aluminium
BHJ	Bulk heterojunction
ETL	Electron transport layer
FTIR	Fourier Transform Infrared Spectroscopy
FPP	Four probe point
FESEM	Field emission scanning electron microscopy
HOMO	Higher occupied molecular orbital
HTL	Hole transport layer
HEM	Hall effect measurement
LUMO	Lower unoccupied molecular orbital
ITO	Indium Tin Oxide
J-V	Current density–voltage
NPs	Nanoparticles
OSC	Organic solar cell
PV	Photovoltaic
PCS	Perovskite solar cell
P3HT	Poly (3-hexylthiophene)
PCBM	[6 ,6]-Phenyl-C7i-butyric acid methyl ester
PEDOT:PSS	Poly(3,4-ethylenedioxythiophene)- poly (styrene sulfonate)
RMS	Root mean square
Si	Silicon
UV-VIS- NIR	Ultraviolet-visible spectroscopy-near infrared
XRD	X-ray diffraction
ZnO NPs	Zinc oxide nanoparticles
1,2-DCB	1,2-dichlorobenzene
2,3-DHP	2,3- Dihdropyran

SEL SURIA ORGANIK BERASASKAN P3HT:PCBM DIGABUNGKAN ADITIF PEPEJAL UNTUK APLIKASI FOTOVOLTA DALAMAN

ABSTRAK

Dengan pertumbuhan pesat Internet benda (IoT), sel suria organik (OSCs) semakin digunakan untuk aplikasi dalam ruang kerana rekabentuknya yang ringan, mudah diproses, dan mudah disesuaikan dengan persekitaran dalaman. Namun, kawalan morfologi tetap mencabar disebabkan oleh variasi dalam kinetik pengeringan filem melalui pelbagai kaedah fabrikasi. Baru-baru ini, aditif pepejal menunjukkan potensi untuk memperbaiki morfologi, memperkembangkan proses rawatan pasca, dan meningkatkan kestabilan, menjadikannya pendekatan yang dipilih untuk mengoptimalkan OSCs. Oleh itu, kajian ini tertumpu kepada fabrikasi OSCs berasaskan P3HT:PCBM-C71 yang disertakan dengan aditif pepejal (2,3-DHP) untuk aplikasi fotovoltan dalaman (IPV), menggunakan PEDOT:PSS sebagai lapisan pengangkutan lohong (HTL) dan ZnO NPs:Alq₃ sebagai lapisan pengangkutan elektron (ETL). Kajian ini dibahagikan kepada empat bahagian utama: Pada bahagian pertama, pengoptimuman komposisi dicapai dengan menyesuaikan kepekatan P3HT dan PCBM menggunakan teknik pemrosesan larutan. Morfologi dan kehabluran terbaik diperhatikan dalam campuran nisbah 1:1 menggunakan pelarut bersama 1,2-diklorobenzena (DCB), yang disepulindap pada suhu 100 °C, menghasilkan PCE 1.7%. Bahagian kedua menumpukan pada meningkatkan kekonduksian PEDOT:PSS dengan menambahkan aditif pepejal seperti 2,3-Dihidroksipiridina (2,3-DHP). Gabungan PEDOT:PSS@2,3-DHP menghasilkan PCE melebihi 3%. Dalam bahagian ketiga, PCE yang lebih tinggi melebihi 7% diperoleh dengan memasukkan 0.8 wt%

2,3-DHP ke dalam filem campuran P3HT:PCBM. Kesan pelbagai ETL juga dikaji, termasuk ZnO NPs, Alq3, dan gabungan keduanya. Kombinasi ZnO NPs:Alq3 sebagai ETL meningkatkan ketumpatan dan pertumbuhan butiran foto-penyerap, mengurangkan perangkap pembawa cas dan laluan kebocoran arus (pembentukan lubang jarum). Bahagian keempat melibatkan penambahan 2,3-DHP ke dalam HTL dan lapisan aktif. Ini menghasilkan lapisan aktif yang padat dengan butiran yang lebih besar, meningkatkan PCE peranti kepada 10%, berbanding peranti rujukan dengan PCE 1.7%, setelah pengoptimuman nisbah 2,3-DHP dalam HTL dan P3HT:PCBM. Prestasi PV dinilai di bawah kematan cahaya dalaman dari 10% (4.4 mW/cm²) hingga 100% (44 mW/cm²), memberi tumpuan kepada kesan 2,3-DHP pada morfologi, struktur, dan PVs. Tanpa aditif, peranti menunjukkan kecekapan terendah, dengan PCE 0.01% pada 10% cahaya dan 1.72% pada 100%. Penambahan 2,3-DHP ke dalam HTL meningkatkan PCE kepada 0.29% pada 10% cahaya dan 3.67% pada 100%, manakala penambahan ke dalam P3HT:PCBM meningkatkan PCE kepada 0.83% pada 10% dan 7.36% pada 100%. Penambahan 2,3-DHP ke dalam kedua-dua HTL dan lapisan aktif mencapai PCE tertinggi, dengan 2.52% pada 10% cahaya dan 10.4% pada 100%, mengatasi semua konfigurasi lain. Ciri J-V yang konsisten pada pelbagai kematan menunjukkan kesesuaian peranti ini untuk aplikasi dalaman, menawarkan pendekatan terbaik ke arah sel suria yang cekap dan tahan lama untuk kegunaan IPV.

**P3HT:PCBM-BASED ORGANIC SOLAR CELLS INCORPORATED
WITH SOLID ADDITIVES FOR INDOOR PHOTOVOLTAIC
APPLICATIONS**

ABSTRACT

With the rapid rise of the Internet of Things (IoT), organic solar cells (OSCs) are increasingly sought for indoor applications due to their lightweight design, easy fabrication, and adaptability to indoor settings. However, morphology control of the OSCs remains challenging due to variations in film-drying kinetics across fabrication methods. Recently, solid additives have shown promise in improving morphology, streamlining post-treatment, and enhancing stability, making them a preferred approach for optimizing OSCs. Therefore, this study focused on fabricating P3HT:PCBM-C₇₁-based OSCs incorporated with solid additives (2,3-DHP) for indoor photovoltaic (IPV) applications, using PEDOT:PSS as a hole transport layer (HTL) and ZnO NPs:Alq₃ as an electron transport layer (ETL). The work was divided into four main parts: In the first part, composition optimization was achieved by adjusting the concentration of P3HT and PCBM using a solution-processing technique. The optimal morphology and crystallinity were observed in the 1:1 ratio blend using a co-solvent of 1,2-dichlorobenzene (DCB) annealed at 100 °C, resulting in a power conversion efficiency (PCE) of 1.7% (as a reference device). The second part focused on enhancing the conductivity of PEDOT:PSS by adding solid additives like 2,3-Dihydropyridine (2,3-DHP). Combining PEDOT:PSS@ 2,3-DHP resulted in a PCE exceeding 3%. In the third part, a higher PCE of above 7 % was obtained by incorporating 0.8 wt% 2,3-DHP into P3HT:PCM blend films. The effect of different ETLs, including ZnO NPs, Alq₃, and a hybrid of both, was investigated. The

combination of ZnO NPs:Alq3 as ETL further enhanced the compactness and grain growth of the photo-absorber, leading to a further reduction in charge carrier traps and current leakage paths (pinhole formation). The fourth part involved adding the 2,3-DHP to both the HTL and active layer. This led to the growth of a densely packed active layer with larger grains, promoting the device PCE to 10% by optimizing the ratio of 2,3-DHP in the HTL and P3HT:PCBM, respectively, compared to the reference device with a PCE of 1.7%. The PV performance was evaluated under various indoor light intensities ranging from 10% (4.4 mW/cm²) to 100% (44 mW/cm²), focusing on the effects of 2,3-DHP on the morphological, structural, and PV properties. The device showed the lowest efficiency without additives, with PCE of 0.01% at 10% light and 1.72% at 100%. Adding 2,3-DHP to the HTL led to the PCE of about 0.29% at 10% light and 3.67% at 100%, while incorporating it in P3HT:PCBM raised the PCE to 0.83% at 10% and 7.36% at 100%. Introducing 2,3-DHP into the HTL and active layer achieved the highest PCE, with 2.52% at 10% light and 10.4% at 100%, outperforming all other configurations. Consistent J-V characteristics at varying intensities indicate these devices' suitability for indoor applications, presenting a promising approach to efficient, durable solar cells for IPV applications.

CHAPTER 1

INTRODUCTION

1.1 Introduction

The increasing importance of clean energy as a replacement for depleting non-renewable resources like fossil fuels has resulted in exceptional demands for energy-harvesting systems based on renewable energy sources [1], [2]. Organic solar cells (OSCs) are among photovoltaic (PV) technologies that hold the promise of providing energy to support the Internet of Things (IoT) ecosystem including remote sensors, calculators, smart meters, wearable devices, and communication devices. The OSCs are increasingly being adopted in various applications such as smart homes, factories, offices, and wearable technologies (Figure 1.1) [3], [4].

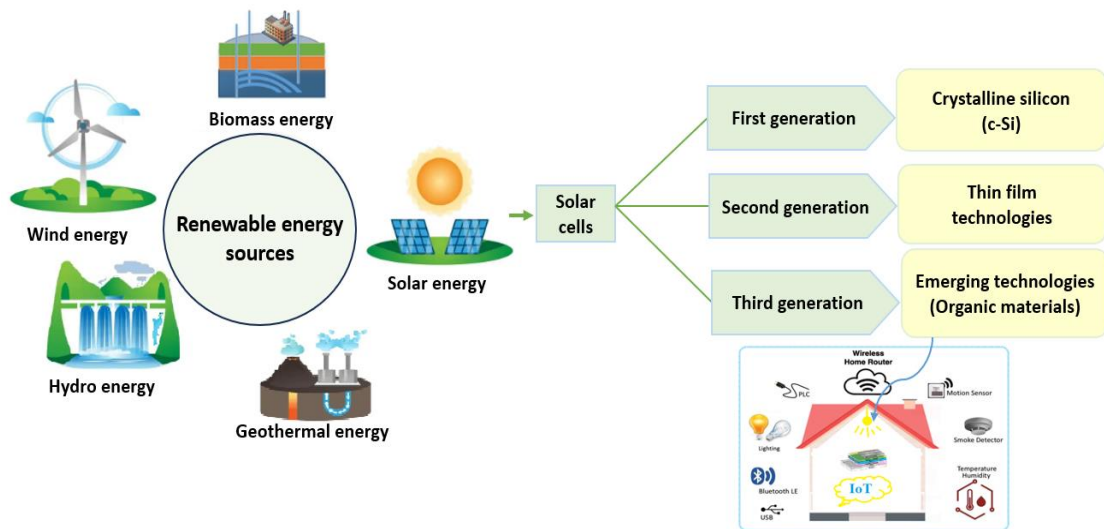


Figure 1.1 Various renewable energy resources and solar energy conversion into electricity by different generations of PV technologies.

The remarkable attributes of OSCs, including their eco-friendly, mechanical flexibility, cost-effectiveness, lightweight nature, ease of fabrication, and transparency, would pave the way for a significant market opportunity. The increasing demand for self-powered microelectronic indoor photovoltaic (IPV) devices would

further amplify this opportunity, creating a favorable landscape for current and future PV technologies [5].

OSCs are capable of harvesting indoor light into output electrical which is suitable for powering electronic devices [6]. Although OSCs offer numerous advantages, they face challenges primarily related to the thickness of their active layer, typically ranging from 100-200 nm. This limited thickness leads to restricted light absorption, as depicted in Figure 1.2, and short carrier exciton diffusion lengths due to constrained hopping transport. Moreover, stability concerns arise when energy harvesting technologies are used in outdoor applications, as they are vulnerable to solar radiation. Additionally, the large-scale fabrication of these technologies presents additional challenges. However, there is still a limited understanding of the exact relationship between device characteristics and material performance, and several parameters are yet to be fully understood [6], [7].

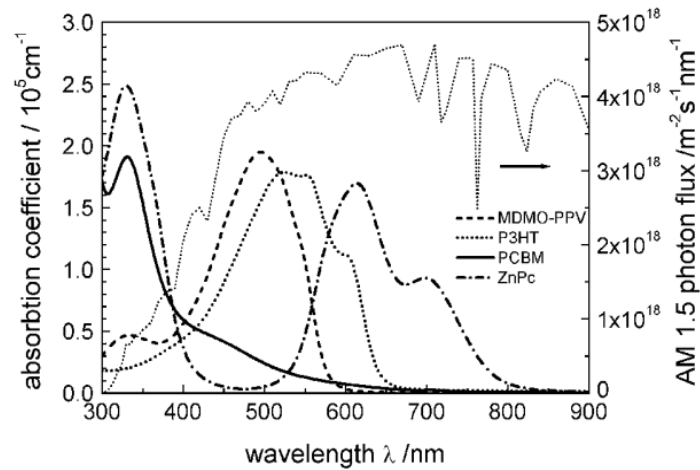


Figure 1.2 Absorption coefficients of utilized donor and acceptor materials [8].

In general, OSCs can convert indoor illumination into energy more effectively than other inorganic technologies. This is owing to OSCs' highly adjustable optical absorption, significant absorption coefficient, and low leakage currents, especially under low-light conditions [8]–[10]. Compared to the typical solar spectrum, the

emission spectra of indoor illumination sources are far more constrained due to their design, which prioritizes energy efficiency and human visual needs, resulting in a narrower and more selective range of wavelengths. Accordingly, their irradiance intensities are around 1000 times lower than outdoor light from one sun [11], [12]. Thus, indoor light sources have considerably different spectra, composition, and illumination intensities. Figure 1.3 shows the typical power consumption of various personal devices and mainstream wireless networks ranging from 1 μ W to 1 W, demonstrating that IPVs are attractive options for harvesting energy in low-light conditions [3], [13].

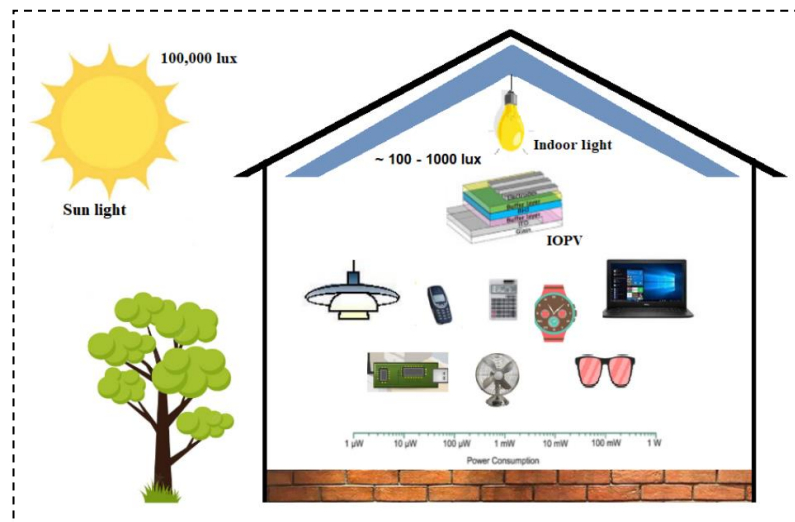


Figure 1.3 Standard household and personal electronics and common wireless network protocols, all contribute to low power usage.

Furthermore, regarding indoor power generation, OSCs outperform c-Si solar cells with higher open circuit voltage (V_{oc}) and a more suitable absorption spectrum. Indoor organic photovoltaic (IOPV) cells have power conversion efficiencies (PCEs) exceeding 35% using light-emitting diodes (LEDs) lamps with intensities ranging (100-1700 lux), and about 17% under 1-sun irradiation (standard test condition). In comparison, c-Si solar cells have achieved PCEs of around 20% under LED lighting conditions [10], [14]. Figure 1.4 illustrates the spectra of various commonly used

indoor lighting sources, such as LEDs, fluorescent (FL) bulbs, and halogen lights. These artificial lighting sources have the potential to generate sufficient energy to power most low-power consumption indoor electronic devices [3].

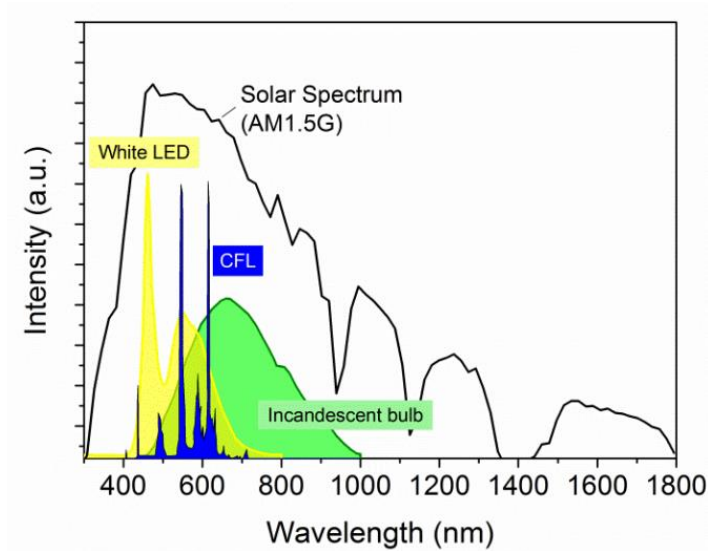


Figure 1.4 Different light spectra: solar spectrum (AM1.5G), white LED, CFL, and Halogen sources [15].

To date, various reviews have been reported on active layer materials and have highlighted active layer materials achieving V_{oc} values as high as 1.0 V and J_{SC} values up to 20 mA/cm² [16]–[18]. The growing demand for energy-autonomous applications is set to boost the IPV market, with a projected 10-15% growth in micropower (use of very small amounts of electrical power, typically in milliwatts or microwatts), which are ideal for powering low-energy devices like Internet of Things (IoT) devices, wireless sensors, electronic shelf labels, smart thermostats, and wearable health monitors. In 2017, the commercial market for IPV was valued at approximately \$140 million, significantly lower than the \$100 billion market for solar power devices. However, due to the escalating demand for IPV applications, the market for IPV is expected to experience substantial growth. Analysts project that the global market for IPV will exceed \$368 billion annually by 2030 (see Figure 1.5), with potential for further expansion in the years to come [3].

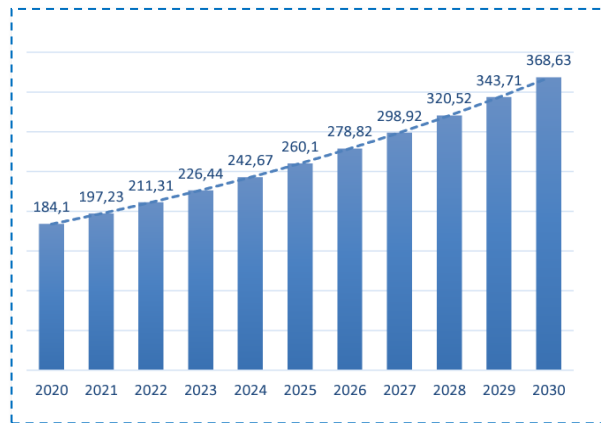


Figure 1.5 Market size of IOPV in billions of dollars [19].

Following subsequent advancements, significant progress was achieved in the field. Wang et al. made noteworthy improvements, resulting in the current state reaching a high PCE of 35.2%. The incorporation of an ionic liquid, [BMIM]BF₄, enabled this achievement by effectively passivating surface traps and facilitating favorable electron extraction and transportation [20]. These enhancements were observed under an illumination intensity of 1000 lux from an FL lamp.

The continuous growth and progress of IPV across various material aspects demonstrate a clear trend. To achieve improved PCEs and enhanced stability of IPVs, researchers must comprehensively understand device characteristics and the materials developed to date [21]. The discovery and development of light-absorbing materials have made a substantial contribution to this advancement. Beginning with basic single polymer donors and fullerene derivatives as acceptors with increased optoelectrical properties, such as light absorption, exciton generation, and charge transportation, has been presented [22], [23].

Furthermore, with the tremendous advances made in light-absorbing materials, innovative device designs like a ternary active layer for IPV have garnered growing interest. Significant progress has also been achieved, such as electrodes and interlayers

[24], [25]. And, as the drive towards clean, green, and renewable energy continues to advance, IOPV can highlight the importance of clean and reliable energy in the advancement of the Sustainable Development Goals (SDGs) 7 (Affordable and Clean Energy), 9 (Industry Innovation and Infrastructure), 11 (Sustainable Cities and Communities), and 13 (Climate Action).

1.2 Problem statement

Highly efficient, stable, and easily prepared OSCs hold tremendous promise as a sustainable power source. The performance and degradation of OSCs depend largely on the morphology of the active layer and the quality of the sublayer, such as the hole transport layer (HTL) and the electron transport layer (ETL). Improving these layers is crucial for better device performance. Low-temperature processed PEDOT:PSS is a good candidate for HTL because it is transparent in the visible range and works well with the active layer. However, PEDOT:PSS can absorb moisture and is acidic, which can lead to degradation and reduced OSC performance [26], [27].

To solve these problems, researchers have tried different methods, such as doping and adding additives to PEDOT:PSS to improve the interface between HTL and the active layer. A bulk heterojunction (BHJ) structure can help improve efficiency by better separating excitons into electrons and holes. However, further improvements in material properties, such as broad absorption spectra and high carrier mobility, are needed to achieve higher efficiency. Moreover, advances in small organic molecules and polymers, both non-fullerene and fullerene acceptors, have significantly improved OSCs [26]–[28]. Still, the efficiency of OSCs is lower than that of inorganic solar cells, mainly because organic semiconductors have a higher band gap (1.8 to 2.0 eV) and are more sensitive to oxygen, moisture, and heat [27], [29]. It is realized that active

material morphology, thickness, and interface design are key to overcoming the energy loss. For efficiency–transparency trade-off lessening purpose, thin active materials and interface, their morphology, crystallinity, and carrier selectivity are the main requisites [30]–[32].

This study aims to improve the morphology of PEDOT:PSS buffer layer and P3HT:PCBM-BHJ OSCs by adding 2,3-DHP. The interaction between 2,3-DHP and PEDOT:PSS is expected to change the mechanical properties of PEDOT:PSS, improving its structural and electrical characteristics. The chemical structure of 2,3-DHP, which has a pyridine group and two hydroxyl groups, allows it to interact well with P3HT and PCBM. This can improve the structure of the active layer, making it better at separating excitons and transferring charges. Thus, it is becoming increasingly important to understand how the properties of solid additives affect active layer morphologies to streamline the selection process for these blends. As, incorporating solid additives such as 2,3-DHP is expected to stabilize the morphology, crystallinity, and light absorption of the active layer, thus increasing the efficiency, J_{sc} , and FF of the device without affecting the V_{oc} .

Furthermore, low-temperature processed ZnO NPs as ETL in OSCs are gaining attention due to their high charge mobility and cost-effectiveness. ZnO NPs enhance the electrical properties of the ETL because of its high charge mobility, transparency in visible light, and good compatibility with the active layer. It also ensures good percolation pathways for charge carrier transport to the appropriate electrodes. It reduces free charge recombination before reaching the interface layer of electron donor-acceptor materials within the diffusion length, generally around 20 nm in organic materials, which is critical for optimizing OSC performance [27], [33]. However, ZnO NPs-based ETLs are particularly problematic due to poor morphology

and chemical stability at the ZnO NPs/active layer interface, which hinders charge transfer. This instability is related to residual organic species on the surface of low-temperature processed ZnO NPs ETL, leading to deterioration in OSC performance. Various strategies, such as the doping process, here in this study, doping ZnO with Alq3 to prepare nanocomposite ETLs, have been adopted to improve the interface and enhance OSC performance. Nonetheless, creating efficient OSC processes remains challenging and requires further research.

1.3 Research focus

Various parameters, including the types of substrates, electrodes, HTLs, ETLs, the concentration and type of the active layer materials, and the overall architecture of the OSC influence the performance of OSCs. Additionally, the quality of the HTL/active layer and active layer/ETL interfaces plays a crucial role in the mechanism of photogenerated charge carrier transfer, stability, and overall performance of OSCs. This thesis focuses on preparing efficient low-temperature processes of sublayer PEDOT:PSS@2,3-DHP as HTL and ZnO NPs ETLs and incorporating Alq3 as an ETL. Furthermore, the study investigates the use of 2,3-DHP in P3HT:PCBM separately and in the HTL with active layers, respectively, to enhance the PCE and stability of OSCs. By engineering the HTL/active layer/ETL interface and optimizing the use of solid additives, this research aims to achieve significant improvements in the performance and durability of OSCs (Figure 1.6).

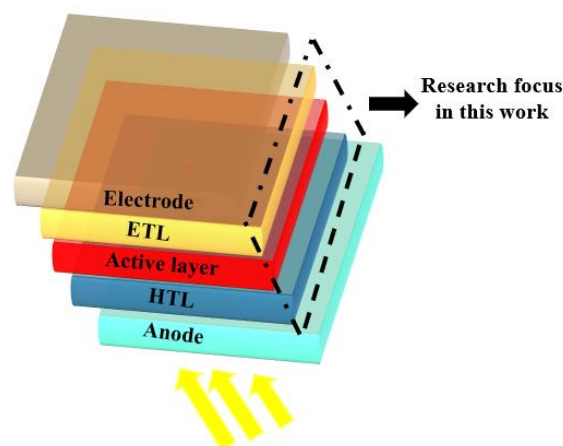


Figure 1.6 Schematic device illustration of the research focus of this thesis.

1.4 Research objectives

The objectives of this work are as follows:

1. To synthesize an organic absorber layer based on P3HT:PCBM using a solution-processing technique.
2. To enhance PEDOT:PSS and active layer morphology, using functional solid additive (2,3-DHP).
3. To optimize ZnO NP-based films doped with Alq3 as an efficient ETL for OSCs by improving their morphology, optical, and electrical properties.
4. To evaluate the conversion efficiency of OSCs under low illumination conditions (typically ranging from 10% (4.4 mW/cm^2) to 100% (44 mW/cm^2)) for IPV applications.

1.5 Thesis outline

This thesis consists of five chapters. In chapter 1, the research highlights the problem statement, objectives, contribution, and scope of the study. Chapter 2 delves into the theoretical background, elucidating the concept of OSCs, its working principle, solid additives, and relevant prior research. Chapter 3 centers on the

materials utilized, the synthesis of buffer layers, OSC fabrication, and characterization processes. Chapter 4 presents and discusses the results obtained from the study. Finally, Chapter 5 concludes, summarizes the findings, proposes future enhancements to improve OSC efficiency, and suggests potential areas for further research.

CHAPTER 2

THEORETICAL BACKGROUND AND LITERATURE REVIEW

2.1 Introduction

This chapter comprehensively explores PV cells, covering their types, theoretical background, and fundamental properties. It delves into the working principles of both materials and OSC devices. Additionally, the challenges confronting IPVs are thoroughly examined. The materials used as ETL and HTL and their importance emphasize their crucial function and investigate various methods to improve their effectiveness in OSCs. The discussion then shifts to the morphology optimization with solid additives, highlighting their significance in OSC. Furthermore, the chapter presents a literature review, which assesses the performance of OSC when integrated with solid additives. A thorough literature study assesses how well OSCs function when combined with HTL and ETL materials, offering useful insights into their use and improvement.

2.2 Generations of solar cell

According to the materials and their nature, solar cells are separated into four generations (Figure 2.1), with their efficiency record being depicted [34]. Solar cells in the first generation are fairly expensive and are created with good stability and efficiency within 23-27% [35], [36]. This generation includes single-crystalline and multicrystalline silicon solar cells. A single-crystalline silicon solar cell comprises only one crystal on the wafer. On the other hand, a multicrystalline silicon solar cell is composed of several crystal grains on a wafer. Additionally, due to silicon's poor absorption coefficient, solar cells require silicon wafers thicker than 100 μm to achieve effective light absorption. Although monocrystalline solar panels have a higher PCE

than multicrystalline panels, multicrystalline silicon wafer fabrication is simpler and less expensive [36], [37].

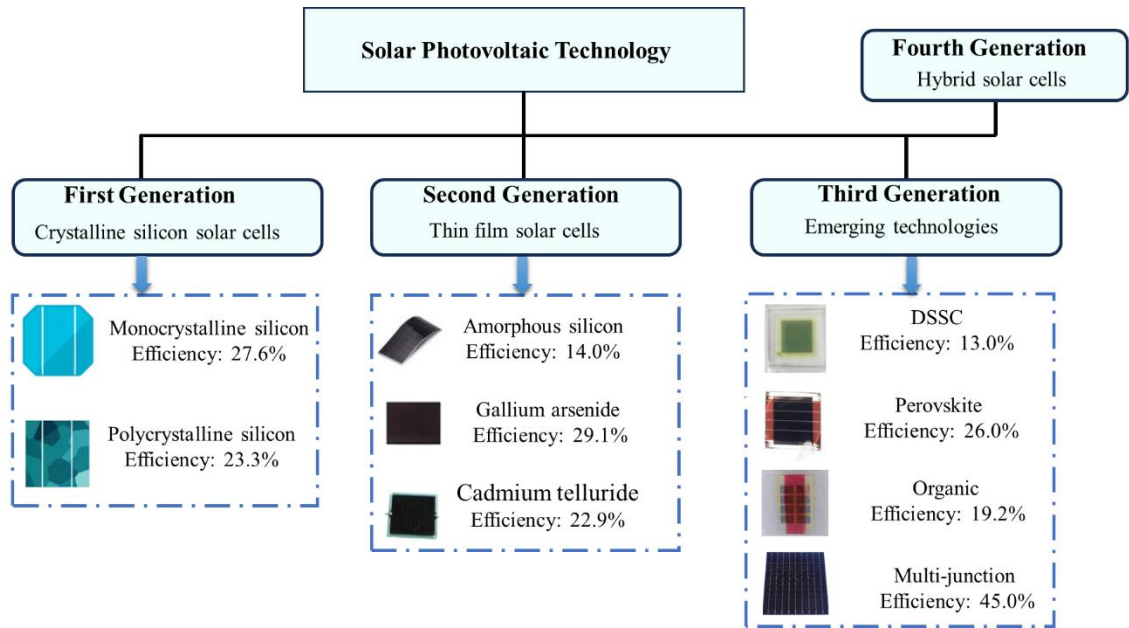


Figure 2.1 Generations of photovoltaics and their types. The maximum reported efficiency, taken from the NREL database [38].

Solar cells from the second generation have an efficiency (14-29%) [37]. They are named second generations because their thickness is much less than the first generation, and they can be as thin as 100 nm. Solar cell generations include thin-film copper indium gallium selenide (CIGS), cadmium telluride (CdTe), and amorphous silicon (a-Si). They can be manufactured on flexible substrates, making them more appropriate for applications like windows, vehicles, and building integrations [37].

High-efficiency thin-film solar cells, such as perovskite solar cells, polymer-based solar cells, dye-sensitized solar cells (DSSCs), and multi-junction solar cells, are used in third-generation solar cells with an efficiency of around (13-45%) [39]. These are ground-breaking innovations that show great promise, but have yet to be commercialized, also have piqued attention due to their simple production process, abundant resources, and low cost. Dye molecules are used to connect electrodes in DSSCs. Dye molecules form electron-hole pairs, which are then transported by ETLs.

OSCs, which have become a viable alternative due to their low cost and excellent efficiency, are one of the most essential types of solar cells due to their light weight, flexibility, and easy preparation [21]. The simplest type is OSC, consisting of an active organic electronic layer sandwiched between electrodes with low and high work functions. Tang et al. introduced a BHJ structure comprising a p-type layer for hole transport and an n-type layer for electron transport to enhance photocurrent in solar cells [40]. However, BHJ devices still face performance limitations due to the low proportion of excitons reaching the heterojunction interface. This limitation is primarily attributed to the short exciton diffusion length (~40 nm); when the active layer thickness exceeds this length, many excitons recombine before reaching the interface, reducing device efficiency [41].

2.3 Organic solar cells (OSCs)

Among various fields of study, renewable energy stands out as increasingly significant and is expected to drive research and development in the coming decades [42], [43]. OSCs represent a promising class of solar cells, that utilize organic materials in their active layers. These materials offer unique characteristics, making OSCs strong contenders for efficient solar energy conversion [44]. As a noteworthy green technology, OSCs have garnered considerable research interest for their potential to address escalating global energy demands by directly converting renewable resources into electricity [45], [46].

The primary distinctions between inorganic and organic semiconductors lie in their electronic structures. Traditional inorganic semiconductors have a crystalline structure where atoms are covalently bonded, and electrons are delocalized over the lattice. The energy levels for these electrons form continuous valence and conduction

bands, separated by a band gap. In inorganic PV cells, light absorption directly elevates electrons from the valence band to the conduction band, creating free charges that can be directed toward the electrodes by applying an external electric potential [47].

In contrast, organic semiconductors combine the electronic properties of semiconductors with the chemical and mechanical benefits of organic compounds, such as plastics. Organic semiconductors are composed of conjugated molecular or polymeric compounds characterized by sp^2 hybridized carbon atoms and unhybridized p_z atomic orbitals. These orbitals form molecular σ and π orbitals, with the bonding (π) and antibonding (π^*) orbitals constituting the highest occupied molecular orbital (HOMO) and the lowest unoccupied molecular orbital (LUMO). Polymeric semiconductors, typically amorphous with macromolecules held together by Van der Waals forces, exhibit narrower bandwidths and weaker delocalization of electronic wavefunctions among neighboring molecules. As a result, the HOMO and LUMO bands in these materials are discrete rather than continuous [48].

In OSCs, light absorption forms tightly bound electron-hole pairs known as Frenkel excitons. These excitons are electrically neutral and must dissociate into free charges at a heterointerface for the solar cell to generate electricity. This process differs from inorganic solar cells, where free charges are directly produced upon light absorption [48], [49].

One of the standout features of OSCs is their high absorption coefficients in the visible range (400-700 nm), allowing for efficient light absorption even with very thin films. Additionally, they can be processed at low temperatures, 60°C , simplifying and reducing the cost of manufacturing. This characteristic enables the production of flexible and lightweight solar cells, suitable for various applications, including curved surfaces and flexible electronics [49], [50].

Despite these advantages, OSCs face several challenges, such as lower efficiency, shorter lifetimes, and faster degradation than inorganic solar cells. Soitec and CEALeti, France, in collaboration with the Fraunhofer Institute for Solar Energy Systems (ISE) in Germany, achieved the highest certified efficiency of about 46% for (GaInP/GaAs and GaInAsP/GaAs) with an active area of 0.0520 cm^2 [51], [52]. To date, PCEs of OSC have exceeded 19%, rapidly approaching the efficiency levels of their inorganic counterparts [53], [54]. This progress is largely due to the development of more effective sublayers (HTLs, ETLs), which play a crucial role in extracting and transporting photo-generated electrons while preventing recombination loss [55], [56].

OSCs are also gaining attention for their potential in IPV applications, efficiently converting indoor light to power small electronic and photonic devices. This capability is particularly relevant with the rise of the Internet of Things (IoT), where numerous low-power devices need reliable energy sources. According to Intel Corporation, there are already 200 billion connected devices, and IoT is expected to generate 55% of all data by 2025 [57].

The cost of generating electricity with PV cells remains higher than fossil fuels. To achieve grid parity, significant reductions in module and installation costs are necessary [58]. OSCs, with their unique properties, offer a compelling alternative when cost and mechanical flexibility are prioritized over high performance or stability. In conclusion, OSCs represent a significant step forward in solar technology, offering a sustainable and versatile solution to meet growing global energy demands. With ongoing research and development, the efficiency and durability of OSCs continue to improve, enhancing their commercial viability and potential to contribute to a green future (Figure 2.2).

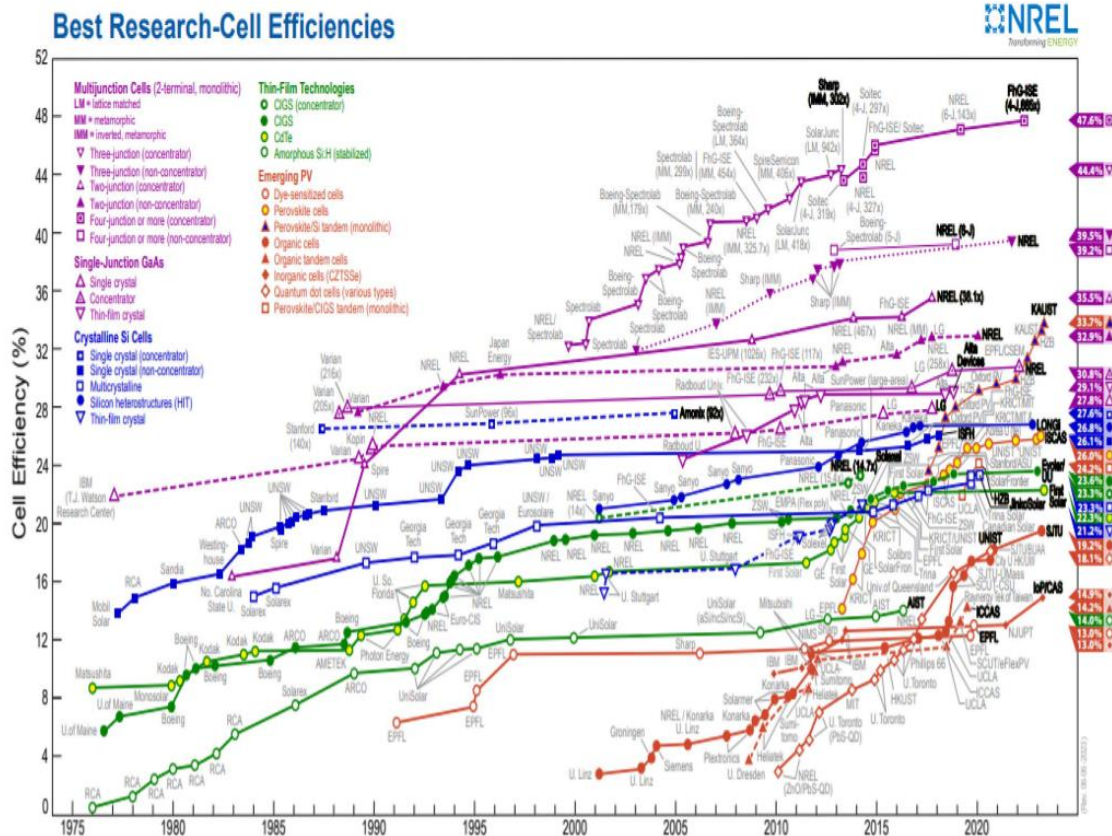


Figure 2.2 The best solar cell efficiency [59].

2.4 OSC device architecture

The basic structure of an OSC is a single organic layer sandwiched between two electrodes or a single-layer cell. When OSC was used in single-layer solar cells, it led to a PCE of around 0.1% and a substantially poor external quantum efficiency (EQE) of roughly 1% [60]. A basic OSC typically consists of two layers: A donor layer and an acceptor layer, which can be configured in various ways, including single-layer, bilayer, or bulk heterojunction (BHJ) structures [61]. Donor-acceptors are brought into proximity in a bilayer heterojunction by sequential deposition of the two layers. The bilayers are positioned between two electrodes to establish an ohmic contact between the acceptor and donor layers. The cathode, located on the donor side, should be both transparent and possess a high work function, commonly achieved using materials like

ITO. On the other hand, the acceptor side is paired with the opposite electrode, known as the anode electrode, which typically has a low WF. The translucent nature of the cathode allows light to pass through the BHJ-active layer [60], [62].

The formation of BHJs (Figure 2.3) through the combination of donor-acceptor organic semiconductor solutions is a critical process in OPVs. During the drying phase, phase separation occurs, influencing the morphology and performance of the resulting thin film. This phase separation leads to the development of a more favorable interface and a reduced diffusion distance for exciton separation. As a result, the formation of nanoscale interlayers through spontaneous phase separation can improve the efficiency and stability of devices by reducing contact resistance. The photo-generated exciton in a BHJ OSC has a higher probability of diffusing to a neighboring interface, where it can undergo dissociation and provide continuous pathways for charge transport. This process has led to a substantial increase in device performance. As a result, the PCE of BHJ OSC cells has exceeded 18% according to studies [63], [64]. This significant improvement in PCE has generated increased interest in OSC research, as the efficiencies achieved through the BHJ design surpass those obtained from the bilayer structure [65].

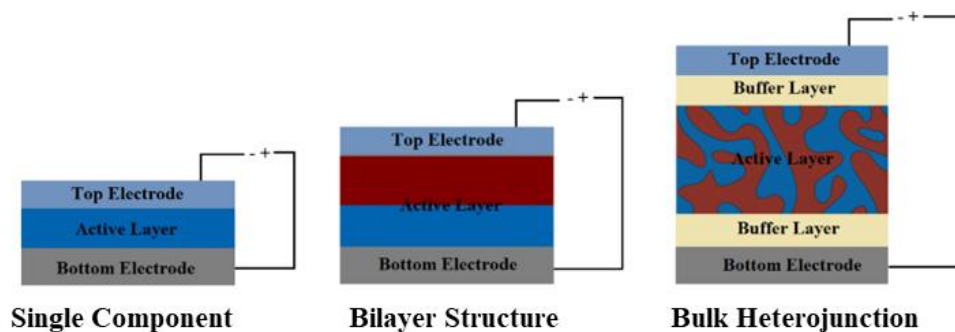


Figure 2.3 The OSC configurations.

2.4.1 Bulk heterojunction OSCs

The BHJ layer combines the organic material donor with the organic material acceptor, which is the most used configuration (as illustrated in Figure 2.4 (b)) in the fabrication of OSCs [65]–[67]. BHJ-OSCs offer suitable donor-acceptor interfaces with nanoscale phase separation, creating interpenetrating networks for efficient exciton dissociation and charge carrier transport. This unique architecture overcomes the limitations of short exciton lifetime and diffusion length in OSCs [68].

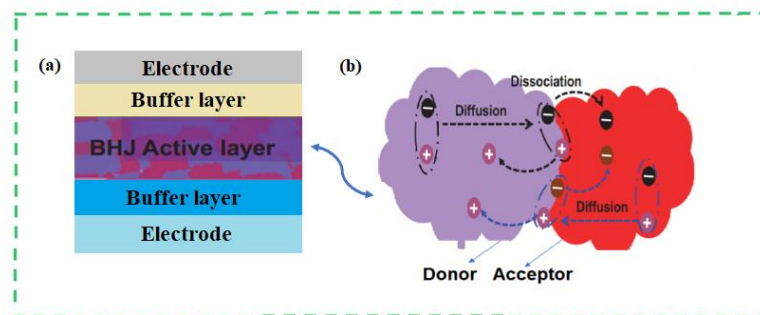


Figure 2.4 (a) OSC device configuration, (b) Blend of the BHJ active layer.

BHJ solar cells, introduced by Heeger et al. in 1995 [67], [69], to optimize the OSC performance (Figure 2.5). It is crucial to minimize resistance, establish efficient ohmic contact, and ensure superior charge selectivity at the interfaces [70]. Significant progress has been made in the development of BHJ-OSC architectures. In which inverted devices outperform conventional solar cells with standard architectures while providing improved environmental stability [71], [72].

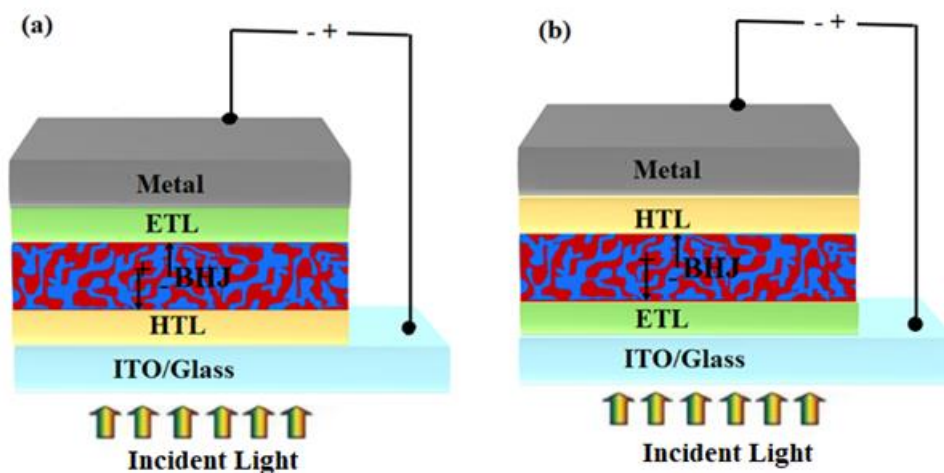


Figure 2.5 Device architecture for (a) Conventional, and (b) Inverted OSCs.

2.4.2 Buffer layers in OSCs

Both conventional and inverted OSCs require buffer layers with low WFs to align the acceptor material's LUMO level for efficient charge extraction. Additionally, HTLs possess excellent hole-transporting and electron-blocking properties to facilitate charge transportation, while ETLs should possess excellent electron-transporting and hole-blocking properties to facilitate charge transportation. Furthermore, they should be compatible with both the electrodes and active layers to protect the absorber layer from degradation caused by environmental factors such as moisture (Figure 2.6). Meanwhile, it is crucial for ETL in inverted OSCs to have high transparency for light transmission and to be stable to prevent the diffusion of metal electrodes in normal OSCs [73]. The ability to decrease defect states and minimize surface charge recombination is one of the notable modifications of the buffer layers, thereby improving the overall efficiency of OSC devices [74].

Recent studies have demonstrated the effectiveness of novel buffer layer materials and modifications in boosting PCE [75]–[77]. HTL materials are a critical component of OSCs, significantly influencing their PCE and stability. Buffer layer materials used in OSCs can be divided into two main categories: inorganic and organic.

While OSCs incorporating inorganic HTL materials can achieve satisfactory PCE, they face limitations for large-scale commercial roll-to-roll production due to the necessary high-temperature vacuum evaporation process. Moreover, ETLs are crucial in protecting electrical systems, preventing short electrical circuits, and preserving the durability of OSC devices [78], [79]. As a result, the multifaceted role of the interfere layer in OSC devices underscores its importance in achieving high efficiency, and stability.

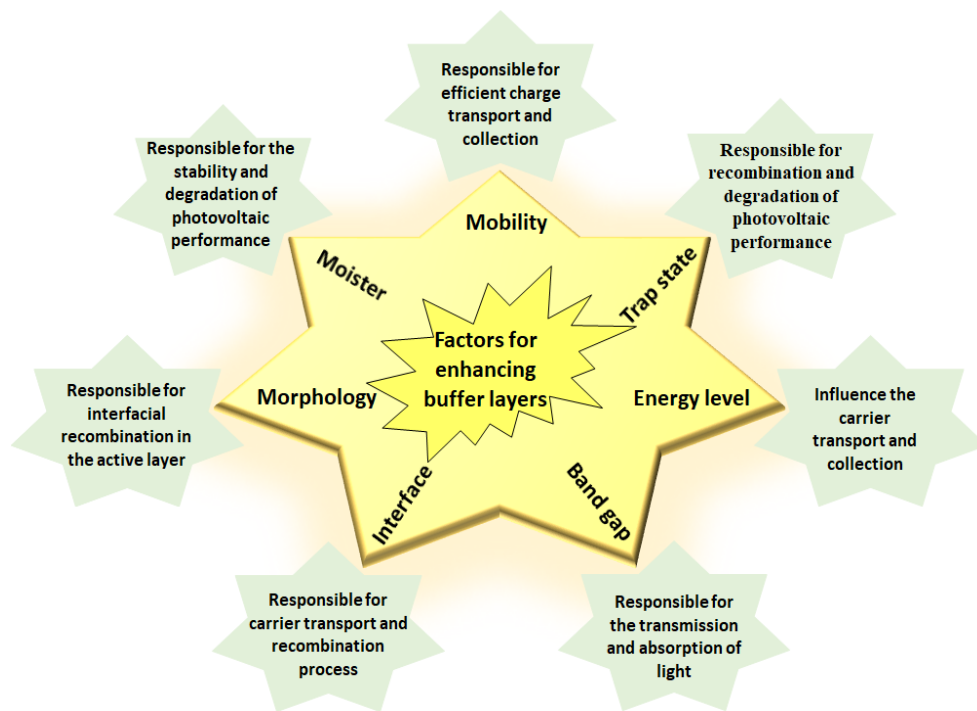


Figure 2.6 Factors for enhancing buffer layers in OSCs.

In OSCs, the creation of nonohmic contact at the electrode/active layer interface can significantly hinder charge collection efficiency and overall device performance. This issue arises when the energy levels of the electrode and the transport layer are mismatched, leading to increased charge recombination and reduced carrier mobility. To mitigate this, strategies such as introducing buffer layers (HTL, ETL), employing suitable work function-modifying materials, or tailoring the morphology of the transport layers are employed to enhance charge transport and achieve efficient ohmic

contact. Therefore, Ohmic contact with electrodes is required to reduce contact resistance, which directly impacts the efficiency of charge injection in devices. Moreover, materials facilitating ohmic contact often serve as buffer layers, preventing the diffusion of metal electrode material into the active layer, thereby preserving the device's structural integrity and long-term stability [24]. The most widely used HTL is PEDOT:PSS, which faces significant challenges due to its instability when exposed to air and mechanical stress. This instability stems from its strong acidity and hygroscopic nature, which can etch the ITO electrode, increasing the mobility of indium [80].

Modifying PEDOT:PSS with additives, for instance, polystyrene nanoparticles (PS NPs) or integrating it with materials like MoO_3 has shown considerable improvements. For example, solar cells with a MoO_3 -PEDOT layer maintained 80% of their original PCE after 240 hours, compared to near-total degradation with unmodified PEDOT:PSS [81]–[84]. Alternative HTLs, including metal oxides like MoO_x and NiO_x or graphene oxide (GO), exhibit lower hygroscopicity and better stability, significantly preserving the efficiency of OSCs over time [85]–[87].

Similarly, ETLs like lithium fluoride (LiF) and calcium (Ca) in conventional geometry, and ZnO in inverted geometry, also suffer from stability issues. LiF and Ca are reactive with oxygen and water, while ZnO is unstable in air and light. Replacing these materials with more stable alternatives, such as metal oxides, stable metals, or modified polymers, can enhance stability. For instance, OSCs with a chromium oxide (CrO_x) ETL preserved 69% of their original PCE after 48 hours, compared to rapid degradation with a LiF ETL. Additionally, modifying ZnO by chemical composition, fabrication methods, or buffer layers has proven effective. $\text{Zn}_{1-x}\text{Mg}_x\text{O}$ (ZMO), for example, significantly improved air stability by acting as a moisture/oxygen scavenger [88]–[92]. Solar cells with ZMO retained their efficiency over a year, while those with

untreated ZnO degraded faster. Surface treatments of ZnO with compounds like ethanedithiol (EDT) or poly-ethylenimine ethoxylated (PEIE) also demonstrated substantial stability improvements. For instance, P3HT/PC₆₁BM solar cells with EDT-treated ZnO preserved 96% of their original efficiency after 720 hours [88]–[92]. Combining these advancements in HTL and ETL materials highlights the potential for significantly improving the stability and efficiency of OSCs, making them more practical for long-term applications. By addressing the challenges of air and light stability through material innovation and modification, the durability of OSCs can be substantially enhanced.

2.4.3 Electrodes in OSCs

The anode is an essential element in the structure of a solar cell, with the primary function of collecting the carriers generated during its operation. ITO and FTO have frequently employed electrodes in optoelectronic devices. These materials are preferred for their low reflection, great transparency, exceptional electrical conductivity, elevated job function, and ease of creating patterns. By serving as the electrodes, they facilitate the extraction of electrons during the flow of an electric current through the device. In the same way, the cathode effectively gathers the produced holes from the absorption layer. When an electric current passes through the OSC, the cathode, which can have different levels of transparency depending on the type of OSC, gathers positively charged holes. Cathodes often utilize highly stable metals with low work functions, including aluminum (Al), silver (Ag), gold (Au), and platinum (Pt) [93][94].

To attain efficient OSCs and gain insight into the fundamental PV mechanisms, it is essential to have a thorough understanding of the fundamental processes occurring inside the layers of the OSCs and the specific role played by each component (Figure 2.7). After electron-hole pairs are generated within the electric field region of the active

layer, they are separated by the influence of the internal electric field. This process directs holes to migrate toward the p-side (anode) and electrons toward the n-side (cathode), enabling their transport to the respective electrodes for efficient charge collection and subsequent electricity generation. The remaining charge carriers are then directed through the external circuit toward the load, where the HTL collects the holes, and the ETL collects the electrons, ensuring efficient charge transfer and minimizing recombination losses [93][94]. Investigating appropriate electrodes is a viable method to enhance mechanical stability [94][95]. For example, Zheng et al. [94] fabricated a composite transparent electrode using graphene as a substitute in OSC. They observed that even after subjecting the graphene-based transparent electrode to 1000 bending cycles, the increase in resistance was only approximately 5%, and no cracks were detected. In contrast, the traditional ITO transparent electrode exhibited a rapid increase in resistance due to the formation of cracks during bending. This demonstrates the superior mechanical flexibility and stability of graphene-based transparent electrodes compared to ITO, making them more suitable for flexible optoelectronic devices [96].

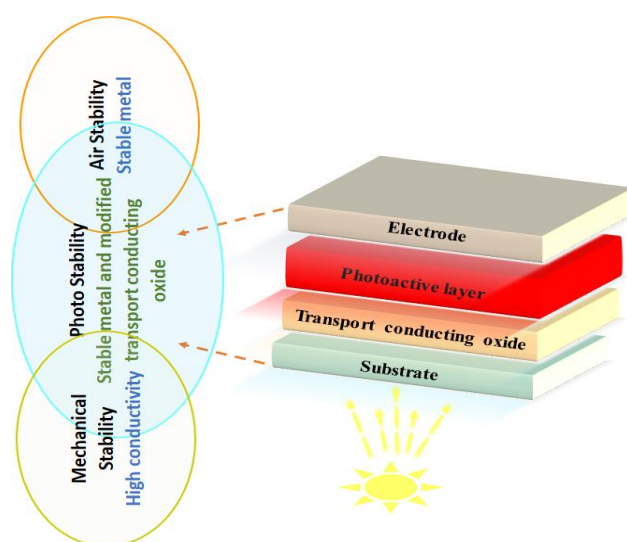


Figure 2.7 Mechanisms of using electrodes for efficient OSCs.

Nevertheless, both ITO and Al demonstrate significant susceptibility to degradation when subjected to mechanical strain, radiation, and exposure to air. Replacing ITO with transparent materials such as metals, alloys, metal nanowires, graphene, polymers, or modified ITO is advantageous for improving stability. Although replacing Al with stable metals like Ag, Au, or Cu, the overall stability of OSCs can be significantly enhanced [96], [97]. For instance, Kim et al. demonstrated that by replacing the Al back electrode with Ag in PTB7/PC₇₁BM solar cells, they achieved a higher PCE than cells with Al back electrodes (8.0% vs 7.1%). This substitution resulted in a notable enhancement in device performance [98].

Similarly, Emrick et al. employed Au as the back electrode in PTB7-TH/PC₇₁BM solar cells and incorporated an innovative electron buffer layer to lower the WF at the Au/active layer interface. As a result, they achieved an impressive PCE of 8.6%, which stood as the highest reported for OSCs with an Au back electrode. This substitution not only improved air stability but also significantly enhanced the device's performance [98]–[100]. Therefore, by replacing Al with stable metals like Ag, Au, or Cu as back electrodes, researchers have achieved better air stability and demonstrated notable advancements in PCE, leading to more efficient and reliable OSCs.

2.5 Operation of OSCs

In general, the process of producing charge from incoming light in OSC cells is divided into four stages [101]. The donor material's electrons are moved from the HOMO to the LUMO energy level of the acceptor material when an OSC absorbs an incoming photon. This process creates holes in the HOMO of the donor. This process leads to the formation of an exciton, a tightly bound electron-hole pair, within the donor-acceptor system. Subsequently, exciton then diffuses and separates at the interfaces